PHYSICAL REVIEW B VOLUME 38, NUMBER 6 15 AUGUST 1988-II

Structures and adsorption energies of commensurate rare-gas monolayers on MgO(100)

T. Meichel and J. Suzanne
Laboratoire des Surfaces-Interfaces, Université d'Aix–Marseille II, Faculté des Sciences de Luminy,
Case 901, 13288 Marseille Cédex 9, France

C. Girard and C. Girardet
Laboratoire de Physique Moléculaire, Université de Besançon, 25030 Besançon Cédex, France

(Received 4 December 1987)

Low-energy electron-diffraction (LEED) measurements of rare-gas monolayers adsorbed on a square-symmetry MgO(100) substrate allow the structure and the isosteric adsorption heat to be determined. The argon monolayer exhibits a typical frustration phenomenon induced by the troughs along the [110] Mg ion rows on the MgO surface. This frustration leads to a $2\times n$ overlayer structure which evolves from $n=3$ to $n=4$ with increasing coverage. For Kr, the coexistence of the $2\times n$ and hexagonal solid phases is observed. Finally, for Xe, LEED shows a hexagonal structure only, with a unidirectional disorder that appears to be induced by the square symmetry of the substrate. Potential calculations are performed to interpret these results by determining the more stable structures and evaluating the isosteric heat of adsorption within the framework of a simplified dynamical treatment of the monolayer atoms. The calculated stable structures are in good agreement with the experimental results for the three rare-gas species. The calculations give a better understanding of the experimental observations, especially by explaining the evolution of the $2\times n$ Ar monolayer structures and the relative stabilities of the different structures of the Kr and Xe monolayers, due to the nonplanar nature of the adsorbate layer.

I. INTRODUCTION

Observations of monolayers of inert gases have been mainly done for hexagonal substrates, the most-studied example being graphite,[1–5] and for the densest faces, (111), of noble metals such as silver[6] and gold.[7] For these species the symmetries of the monolayer and the surface of the substrate are hexagonal and registry effects remain generally weak. Indeed, the experimental results and the calculations indicate[6] that silver produces no detectable registry in the Ar, Kr, and Xe monolayers. On graphite, commensurate phases are observed depending on the physical conditions.

Experimental results are quite different when rare-gas monolayers are adsorbed on substrates with other symmetries than the hexagonal one.[8] An interesting case concerns the adsorption of rare gases on the MgO(100) face, a surface with a square symmetry.[9–14]

The adsorption of rare gases and methane on uniform MgO powders in the monolayer regime has been studied using classical volumetry,[9] neutron-scattering experiments,[10,11] and x-ray diffraction.[12] These experiments have given interesting insights into these systems, but present a main drawback—that is, the impossibility of determining the epitaxial orientation of the adsorbed overlayer due to the scattering of crystallite orientations in the MgO powders. In some cases, it has also been shown that diffraction experiments on powders may lead to an ambiguity in the structure determination and that low-energy electron diffraction (LEED) on single-crystal surfaces is able to remove this ambiguity.

In this paper we present a thermodynamical and structural study of argon, krypton, and xenon monolayers adsorbed on a MgO(100) single-crystal surface using LEED as a probe.[13] A preliminary study has been reported elsewhere in the case of argon and CH_4.[14] Our structural results show that a commensurate phase of the rare-gas monolayer undergoes not only squeezing or expansion of the interatomic spacing, but, in addition, a drastic change in symmetry with respect to the natural hexagonal-close-packed structure. The results for Ar monolayers exhibit a very interesting phenomenon of symmetry frustration between the two-dimensional (2D) hcp packing of the adsorbed phase and the square symmetry of the substrate. Furthermore, isosteric heats of adsorption have been measured from LEED photometric adsorption isotherms for the three gases. Our experimental findings are compared to a theoretical model described below.

The theoretical papers on the study of the monolayer geometry cover two general aspects of the physical processes responsible for the commensurability or incommensurability of the adsorbed phase.

In cases where the substrate surface appears so smooth to the adsorbate that the overlayer forms a 2D lattice incommensurate with the substrate, the free energy of the monolayer can be calculated by separating the 2D dynamics inside the monolayer plane and the motions perpendicular to this plane. The monolayer can then be represented as a floating 2D solid, and quasiharmonic theories[6,15] at low temperature and self-consistent phonon[16] or cell-theory[17] approaches at higher temperature are used to determine the thermal properties of the monolayer, such as the melting temperature. The holding-interaction potential[6] and, in a general way, all quantities connected to the adsorption process on the substrate are then calculated within the framework of a continuum substrate.[18] The atomic vibrations of the monolayer in a plane perpendicular to the adsorbate are nearly dispersionless and they can be regarded as being due to anharmonic identical oscillators.

When registry occurs, the discrete nature of the substrate must be taken into account. An identical geometry for the substrate and the adlayer allows the registry phases or commensurate superlattices to be easily described in terms of the lattice constants. When the lattice structures differ, registry can again occur partially according to geometrical conditions imposed by the lattices. Particular alignments of adlayer and surface-registry directions have been considered by Bruch and Venables[19] from a geometrical point of view. More general orientational alignments have been treated with the perturbation theory[20] and the pseudoharmonic approach,[21] and registry domains have been considered for the intralayer dynamics of incommensurate phases near registry.[22] In contrast with the floating-monolayer model, the approaches incorporating the discrete nature of the two partners need the use of improved interaction potentials which are able to account for the competition between the lateral monolayer interactions and the corrugation of the substrate appearing in the adsorbate-substrate potentials.

We consider in this paper the second aspect with registry effects, with an approach different from those described previously.[19–23] We start with the remark that, on a corrugated surface, the centers of mass of the atoms belonging to the monolayer are located in the same plane for a complete registry only. In opposition, when several adsorption sites occur, i.e., for a partial registry, the monolayer can no longer be considered planar since the atom-surface distance depends on the adsorption site.[24] The periodic characteristics of the monolayer are recovered in the 2D plane over a lattice supercell containing a given number n of atoms ($n > 1$) and defined by the geometries of the monolayer and of the substrate.

This model is expected to be adapted to the cases of substate-adsorbate frustration phenomena, at low temperatures, and for a nearly complete coverage ratio of adsorbate. It may be summarized as follows. Many 2D geometries of the monolayer lattice are chosen to be consistent, on one hand, with the substrate corrugation, and, on the other, with the atomic density of the floating monolayer. These configurations lead to 2D primitive supercells which can be much larger than the cell of the 2D hexagonal or close-packed structures. All the atoms of a supercell in the monolayer, though identical for the floating adsorbate, do not experience the same interaction with the corrugated substrate. Therefore, the holding distances (i.e., the adsorbate-atom–substrate distances) have different equilibrium values connected to the monolayer relaxation perpendicularly to the surface and thus different holding energies. The total interaction potential is then minimized with respect to these distances and the dynamics of the monolayer and substrate is determined for the in-plane and out-of-plane motions of the adatoms. The total adsorption energy per atom for a given configuration is calculated and compared to that of other configurations in order to obtain the most stable monolayer geometry.

Section II is devoted to the compilation of the various contributions of the potential interactions for the adsorbate and the substrate. The equilibrium configurations of the atoms belonging to the monolayer are then determined within the harmonic approximation and the monolayer dynamics is introduced in a simple way to compute the adsorption energy. Applications to Ar, Kr, and Xe monolayers adsorbed on the MgO(100) substrate are done. In Sec. III, LEED measurements on MgO single-crystal surfaces are described. They give structural and thermodynamical information on the various adsorbed monolayers. A comparison between the experimental results and the calculations is presented in Sec. IV.

II. THEORETICAL CONSIDERATIONS

A. The monolayer energy

1. Interaction potentials

The total interaction for a semi-infinite substrate ($z \leq 0$) and an adsorbed monolayer is separated as

$$V = V_M(\mathbf{r}) + V_S(\mathbf{r}_S) + V_{MS}(\mathbf{r}, \mathbf{r}_S) \ . \tag{1}$$

V_M characterizes the interaction contributions between atoms pertaining to the layer and defined by their absolute location vectors $\{\mathbf{r}\}$. V_M appears itself as a sum of pairwise Lennard-Jones or modified Barker potentials given in the literature.[25] Many-body contributions between monolayer atoms are also included through the triple-dipole interaction.[26,27] The analytic form of $V_M(\mathbf{r})$ can be written as an inverse power-series expansion of the distances between atoms.

V_S defines the interactions between ions in the dielectric substrate. These interactions are generally represented as a sum of pairwise ionic terms and of dispersion-repulsion contributions which still depend on the relative distances between ions.[28–30]

The adsorbate-substrate interaction potential V_{MS} contains the binary holding contributions between atoms and ions which can be expressed[29,31–34] in the 2D reciprocal space parallel to the substrate surface as a continuum term characterizing the continuous description of the substrate (as viewed by the monolayer) and as an oscillating term connected to the discrete description of this substrate. The induction contribution due to the polarization of the adatoms by the electrostatic field created by the ionic substrate[34] must also be added to V_{MS}. At last, many-body effects, also called substrate-mediated effects and extensively discussed elsewhere,[35,36] have been included in V_{MS}. The various parameters for V_{MS} are given in Table I.

TABLE I. Constants for the holding and substrate-mediated potentials (in eV Å^n).

	Substrate					
Atom X	$C_6(X\text{-Mg})^a$	$C_6(X\text{-O})^a$	$C_{12}(X\text{-Mg})^a$	$C_{12}(X\text{-O})^a$	$C_{s1}{}^b$	$C_{s2}{}^b$
Ar	13.37	79.58	523 010	3.844×10^6	42.5	30.3
Kr	19.4	115.15	899 769	6.614×10^6	84.66	60.37
Xe	27.95	166.04	1.669×10^6	12.27×10^6	192.3	137.1

[a] Reference 24.

[b] Calculated from the method described in Ref. 36.

2. *The monolayer relaxation*

The influence of the corrugation of the substrate introduces a 3D character to the equilibrium configuration of the monolayer that cannot be considered planar. To calculate the adsorbate configuration, we assume that the substrate is discrete and undeformable and that its surface has the same structure as the bulk geometry. Indeed, experimental[37] and theoretical[38] results have indicated that surface relaxation was very weak for MgO. On the other hand, the adsorbate is formed by a regular arrangement of rare-gas atoms without defects. Among the infinite number of possible arrangements of the monolayer atoms ranging from the structure of the incommensurate hexagonal phase of the 2D rare-gas lattice to the geometry of phases that are commensurate with the substrates, we have to determine the more stable configurations having a periodicity over a relatively small extent. We therefore define a primitive supercell for the monolayer lattice containing n rare-gas atoms. The number and the location of these atoms must obey the two following conditions. The arrangement must be, at least partially, consistent with the substrate geometry in order to minimize the holding interaction through the corrugation contribution. It must, moreover, be sufficiently dense to minimize the intralayer interactions (cf. Table II).

Let $\mathbf{R}(l,s)$ be the 3D location of the sth atom ($s=1,\ldots,n$) of the lth primitive supercell of the adsorbate; the projection of $\mathbf{R}(l,s)$ on the plane (X,Y) parallel to the substrate surface is labeled $\tau^*(l,s)$, whereas the distance of the atom to the surface is defined by $D(s)$. We define $\tau^*(1,1)$, which refers to the absolute position of the origin atom of the first primitive cell, and d^*, which characterizes the equilibrium distance between any monolayer atom and a continuum substrate (i.e., disregarding the corrugation). The quantities $\tau^*(1,1)$ and d^* correspond to the initial conditions of the problem and are calculated in an independent way by minimizing the adatom-substrate interaction potential.[34] The number n and the vectors $\tau(l,s)$ defined by

$$\tau(l,s)=\tau^*(l,s)-\tau^*(1,1) \tag{2}$$

are then varied for realistic monolayer configurations in partial or total registry with the substrate geometry. The interaction potential $V_T=V_M+V_{MS}$ is minimized for each configuration with respect to the distances $D(s)$,

$$D(s)=d^*+z(s)\ , \tag{3}$$

by using the harmonic approximation in the expansion of V_T in terms of $z(s)$. The interaction potential V_T between the first supercell and the whole substrate can thus be expanded as

$$V_T\simeq V_T^0+\sum_s F_T(s)z(s)+\tfrac{1}{2}\sum_{s,s'}\phi_T(s,s')z(s)z(s')\ , \tag{4}$$

where the potential V_T^0 of the 2D monolayer interacting with a continuum substrate, the force $F_T(s)$ experienced by the sth atom, and the force constant $\phi_T(s,s')$ between two atoms s and s' are defined in the Appendix. Note that, for computational simplicity, the mediated and induction contributions are not included in F_T and ϕ_T due to their weak influence. The minimization with respect to $z(s)$ leads to a straightforward formula,

$$\sum_{s'}\phi_T(s,s')z(s')=-F_T(s)\ , \tag{5}$$

which allows us, after inverting the matrix ϕ_T, to determine, from Eq. (3), the positions of the n atoms of the supercell with respect to the substrate surface. An iterative process applied to Eq. (5) is, moreover, performed to ensure the convergence of the solutions by substituting for d^* the value $D(s)$ found at the previous iterative step.

TABLE II. Lattice parameters for 2D rare-gas crystals.

	Atoms		
Parameters	Ar	Kr	Xe
h (Å)	3.86	4.02	4.26
σ (Å^{-2})	0.0775	0.0714	0.062
Θ_D (K)	68.0	61.2	65.7
$\gamma_\parallel$	5.41	4.79	4.17

3. *The monolayer dynamics*

The inclusion of the coupled motions of the atoms of the adsorbate and substrate is made in an oversimplified version of much more improved theories developed for registered monolayers on graphite.[39] A general study of this dynamics is presented elsewhere[40] using the approaches of Refs. 41 and 42. In fact, as mentioned before, the interaction potential represents the main part of the monolayer energy and the dynamical part provides only a small corrective contribution to this energy.

Within the framework of the harmonic description of the monolayer motions, the decoupling approximation of the in-plane and out-of-plane motions of the monolayer atoms, and the assumption of a rigid substrate, the energy connected with the monolayer is written for a primitive monolayer supercell as

$$\mathcal{E} \simeq \mathcal{E}_{\parallel}(T) + \mathcal{E}_{\perp}(T) \;, \tag{6}$$

where the in-plane energy is calculated for a Debye 2D crystal with the characteristic temperature Θ_D,

$$\mathcal{E}_{\parallel}(T) \sim \tfrac{2}{3} nk\Theta_D \left[1 + 6 \left[\frac{T}{\Theta_D} \right]^3 \zeta_3(T) \right] . \tag{7}$$

$\zeta_3(T)$ is the usual temperature-dependent function,

$$\zeta_3(T) = \int_0^{T/\Theta_D} \frac{x^2 dx}{e^x - 1} . \tag{8}$$

For the Debye temperature Θ_D, we use the value of the floating monolayer.[16] Nevertheless, this can be a poor approximation for corrugated substrates since the monolayer atoms can have different adsorption sites and optical modes occur. This problem will be considered in a further paper, but we will mention here that the dynamical contribution appears only as a correcting term to the static potential energy. The energy $\mathcal{E}_{\parallel}(T)$ is easily obtained from the data of Ref. 16 when the influence of the substrate corrugation is neglected. For the out-of-plane energy $\mathcal{E}_{\perp}(T)$, the mean-field approximation is used to describe the motions of the atoms perpendicularly to the substrate surface and the atoms thus behave as independent 1D oscillators with energy

$$\mathcal{E}_{\perp}(T) = \sum_{s=1}^{n} \frac{\hbar}{2} \omega_s \coth \left[\frac{\hbar\omega_s}{2kT} \right] , \tag{9}$$

where $\omega_s = (k_s/M)^{1/2}$ characterizes the frequency of the sth oscillator of a primitive supercell.

4. The adsorption energy

The thermodynamical formulation of the isosteric heat of adsorption of a monolayer adsorbed on a structureless surface substrate has been given by Bruch and collaborators.[43] In their model, the adsorbed monolayer, the 3D perfect gas phase formed by the nonadsorbed species, and the substrate surface are in coexistence in a container of volume V and temperature T and the interactions between the gas and the monolayer are neglected. The heat of adsorption defined as

$$q_{\rm st} = -k \left[\frac{\partial \ln p}{\partial (1/T)} \right]_A , \tag{10}$$

where P is the pressure of the gas and k the Boltzmann constant, can be obtained in terms of the free energy f_M per atom of the monolayer and of its first and second derivatives. This leads to the expression

$$q_{\rm st} = h_G - f_M + T \left[\frac{\partial f_M}{\partial T} + A \frac{\partial^2 f_M}{\partial T \, \partial A} \right] . \tag{11}$$

$h_G = \frac{5}{2} kT$ per atom defines the enthalpy of the perfect gas and A labels the area per lattice site of the monolayer which depends on the monolayer structure in our case.

The calculation of f_M is performed within the same model used to determine $\mathcal{E}(T)$ and V_T. The expression of f_M per atom is obtained, in a straightforward way, as

$$f_M = \frac{V_T}{n} + \frac{kT}{n} \left[\sum_{s=1}^{n} \ln 2 \sinh \left[\frac{\hbar\omega_s}{2kT} \right] + \frac{1}{N} \sum_{j,\mathbf{q}} \ln 2 \sinh \left[\frac{\hbar\omega_{\mathbf{q}j}}{2kT} \right] \right] , \tag{12}$$

where N is the number of primitive monolayer supercells and the latter sum is over the branches j and the wave vectors $\mathbf{q}$ of the 2D monolayer. The isosteric heat per atom is then given by

$$q_{\rm st} \simeq -\frac{1}{n} \left\{ V_T + \mathcal{E}(T) + \sum_s \gamma_s \left[1 - \coth^2 \left[\frac{\hbar\omega_s}{2kT} \right] \right] \left[\frac{\hbar\omega_s}{2} \right]^2 + \frac{1}{N} \sum_{\mathbf{q},j} \gamma_{\mathbf{q},j} \left[1 - \coth^2 \left[\frac{\hbar\omega_{\mathbf{q}j}}{2kT} \right] \right] \left[\frac{\hbar\omega_{\mathbf{q}j}}{2} \right]^2 \right\} + \frac{5kT}{2} . \tag{13}$$

γ_s and $\gamma_{\mathbf{q}j}$ are the Grüneisen parameters for the out-of-plane and in-plane directions. Within the Debye approximation and the hypothesis $\gamma_{\mathbf{q}j} \equiv \gamma_{\parallel}$ for any $(\mathbf{q}, j)$, Eq. (13) can then be written as

$$q_{\rm st} \simeq -\frac{1}{n} \left\{ V_T + \mathcal{E}(T) + \sum_s \gamma_s \left[1 - \coth^2 \left[\frac{\hbar\omega_s}{2kT} \right] \right] \left[\frac{\hbar\omega_s}{2} \right]^2 \right\} - \left[4\gamma_{\parallel} \left[\frac{T}{\Theta_D} \right]^2 \zeta(T) - \tfrac{5}{2} \right] kT , \tag{14}$$

TABLE III. Holding distances (Å) for the atoms belonging to the primitive cell of a monolayer, with selected structures ($n_1 \times n_2$).

Ar (3×2)		2.92		2.99			3.07		2.99	
Kr (3×2)		3.06		3.12			3.19		3.12	
Ar (4×2)	2.91		3.04		3.04	3.04		2.91		3.04
Kr (5×3)	3.07		3.16		3.16	3.24		3.29		3.24
Xe (5×3)	3.13		3.27		3.27	3.39		3.49		3.39

TABLE IV. Static energy (in meV) per atom for various monolayer geometries (cf. Figs. 1–3).

Ar (3×2)	−124.75	Kr (2×2)	−167.2	Xe (2×2)	−205.1
Ar (4×2)	−122.4	Kr (3×2)	−153.5	Xe (5×3)	−182.2
Ar (3×3)	−96.0	Kr (2×8)	−160.5	Xe (3×7)	−176.1
Ar (9×13)	−113.4	Kr (4×7)	−157.1	Xe (5×10)	−195.4

where the function $\zeta(T)$ is given by

$$\zeta(T)=\int_0^{T/\Theta_D}\frac{x^3e^x}{(e^x-1)^2}dx \ . \tag{15}$$

The various constants $\gamma_s, \gamma_\parallel, \Theta_d$ will be discussed in Sec. II B 2.

B. Application

1. General

The investigation of the more stable structures is performed by exploring various monolayer geometries $n_1 \times n_2$ (n_1 and n_2 are integers) with a number density σ (Å^{-2}) close to the density σ_h of the hexagonal structure of the isolated monolayer. Various geometries, for σ around σ_h, consistent with the monolayer arrangement and the substrate periodicity have thus been considered. As the area of the primitive supercell of the monolayer increases, this cell contains more and more rare-gas atoms and hence more and more different adsorption sites. In the limit of very large areas, the structure tends to be hexagonal, i.e., incommensurate with the substrate.

The static energy of the registered monolayer is then minimized for these various structures and the corresponding holding distances connected to the sites in a given supercell are calculated (Table III). The more stable structure is obtained after a comparison of the adsorption energies collected in Table IV. A general trend exhibited by Tables III and IV is the 3D character of the monolayer adsorbed on the MgO substrate. Indeed, excepted for totally commensurate structures with a single adsorption site, the existence of several sites in partially commensurate structures implies that the monolayer is not planar.

The holding potential V_H including the substrate corrugation, the lateral energy V_M of the isolated monolayer, and the many-body interactions V_m are given and compared in Table V.

The dynamics of the monolayer is defined, for the in-plane motions, by the constants given in the literature[16] for the floating monolayer and, for the out-of-plane motions, by the force constants describing the strength of the harmonic restoring force experienced by an adatom and due to the substrate (Table VI). The isosteric heat of adsorption given by Eq. (14) is calculated for the three species of monolayers. These values are collected in Table VII.

2. Argon monolayer

Figure 1 and Table IV show that the most stable structure is the 3×2 one, with a calculated static energy equal to −124 meV. This structure is slightly less dense than the isolated monolayer structure and it contains four atoms in a primitive supercell. Among the four adsorption sites, two are equivalent, and thus three unequivalent sites are obtained with different static energies. Figure 1 shows that these four sites are located on Mg troughs and define preferential adsorption directions in the (X,Y) plane. This result is in agreement with previous results that showed[24] that the most stable sites for an isolated rare-gas adatom were the Mg sites. This is also consistent with the idea that the corrugation effect is minimized when a maximum number of atoms is located in Mg sites.

The 4×2 structure, also investigated, is a bit more dense than the hexagonal structure and than the 3×2 structure and appears more energetic (less stable). Table

TABLE V. Contributions of the interaction potential for a monolayer atom (in meV).

Ar				Kr				Xe			
(Structures) density	V_H [a]	V_M [b]	V_m [c]	(Structures) density	V_H	V_M	V_m	(Structures) density	V_H	V_M	V_m
(3×2) $\sigma=0.075$	−97.9	−30.4	3.6	(2×2) $\sigma=0.056$	−133.9	−38.6	3.98	(2×2) $\sigma=0.056$	−163.0	−49.7	7.9
(4×2) $\sigma=0.084$	−97.8	−29.1	4.5	(3×2) $\sigma=0.075$	−126.5	−34.1	6.8	(5×3) $\sigma=0.045$	−140.9	−45.0	4.7
(3×3) $\sigma=0.05$	−84.6	−16.0	1.49	(2×8) $\sigma=0.70$	−130.8	−37.2	7.5	(3×7) $\sigma=0.042$	−141.7	−38.9	4.5
(9×13) $\sigma=0.077$	−82.0	−35.2	3.8	(4×7) $\sigma=0.072$	−123.7	−22.7	8.19	(5×10) $\sigma=0.063$	−141.5	−63.5	9.5

[a] The holding energy V_H is defined as $V_H=\bar{v}_b+\tilde{v}_b+v_i$.

[b] V_M labels the energy of the isolated monolayer per atom.

[c] V_m characterizes the substrate-mediated energy.

TABLE VI. Harmonic force constants (in meV Å $^{-2}$) for the perpendicular motions of the monolayer atoms. The numbers in parentheses label sites defined in Figs. 1–3.

Ar (3×2)		394.9(1)	241.6(2)		301.6(3)	301.6(4)
Ar (3×3)		398.8(1)	262.8(2)		257.2(3)	262.8(4)
Kr (3×2)		293.7(1)	216.0(2)		238.5(3)	238.5(4)
Kr (5×3)	355.9	300.9	300.9	336.9	540.9	336.9
Xe (5×3)	607.3	407.5	407.5	349.6	405.7	349.6

V shows a larger contribution of the substrate-mediated energy ($V_m > 0$), indicating a compression of the hexagonal structure of the monolayer. In contrast, the 3×3 structure yields a large dilatation of this hexagonal structure since $\sigma \sim 0.05$ Å$^{-2} < \sigma_h$, and V_m tends to vanish ($V_m \sim 1.5$ meV).

When structures close to the hexagonal density are investigated by choosing much larger primitive supercells (9×13, for instance), the lateral energy becomes optimized, but the registry defect with the substrate is maximum and, as a consequence, it reduces the corrugation term. The energy loss due to the loss of corrugation, as viewed by the monolayer, is about 18 meV and leads to a less stable structure than the 3×2 and 4×2 ones.

Improvements in the calculation of the adsorption energy are introduced by calculating the harmonic force constants connected to the motions of the adatoms along the direction perpendicular to the substrate surface. The values of these constants given in Table VI can be very different—by about 40%—from the more stable site, which is more harmonic than the less stable one. The Grüneisen constants γ_s for the various atoms of the supercell are assumed to remain very small since the main contribution to the frequency ω_s is due to the holding interaction and not to the lateral, area-dependent, energy. The terms proportional to γ_s will then be neglected. For the 2D in-plane motions, the selected value of the Debye temperature is that of Ref. 16 and corresponds to the floating monolayer (Table II). The Grüneisen parameter $\gamma_\parallel$ is, in contrast to γ_s, relatively important since the 2D frequencies are very sensitive to the lateral interactions.

3. *Krypton monolayer*

The 2×2 and 2×8 structures have been found to be the most stable with static energies −167 and −160 meV, respectively (cf. Fig. 2). The first structure corresponds, nevertheless, to a slight dilatation of the isolated monolayer, whereas the second structure has a number density close to the hexagonal one. With respect to the 2×2 structure, the 2×8 one exhibits a corrugation loss, but a gain in the lateral interaction. In fact, the krypton monolayer appears to be relatively stable for a lot of structures with large primitive cells (for instance, the 4×7 structure, with a static energy equal to −157 meV).

4. *Xenon monolayer*

The most stable structure is the square 2×2 one, the static energy being equal to −205 meV (Table IV and Fig. 3). Such a structure is totally commensurate with the substrate since there is only one adsorption site (the Mg site). The stability of the 2×2 structure is due to the importance of the corrugation, which contributes 20 meV to the static energy.

A more compact structure, close to the hexagonal one, for instance, the 5×10 structure (Fig. 3), could eventually compete with the 2×2 one because the energy gain due

TABLE VII. Isosteric heat of adsorption q (in kcal mol^{-1}) for the rare-gas monolayers.

	Calculated	Experimental
Ar ($T=30$ K)	2.33	2.3
Kr ($T=44$ K)	2.91	3.05
Xe ($T=60$ K)	3.70	3.8

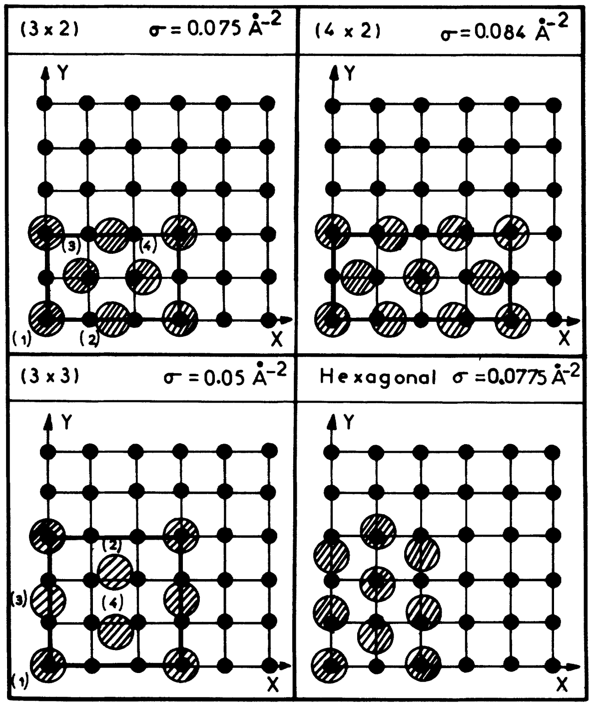

FIG. 1. Selected structures ($n_1 \times n_2$) of the Ar monolayer adsorbed on the MgO(100) substrate. The solid circles characterize the Mg sites; the oxygen sites are located at the centers of the squares. The primitive supercell for the monolayer is drawn: the rare-gas atoms are schematized by larger circles with oblique lines.

to the increase of the lateral energy could nearly balance the loss of corrugation. Other investigated structures are less stable (Table IV).

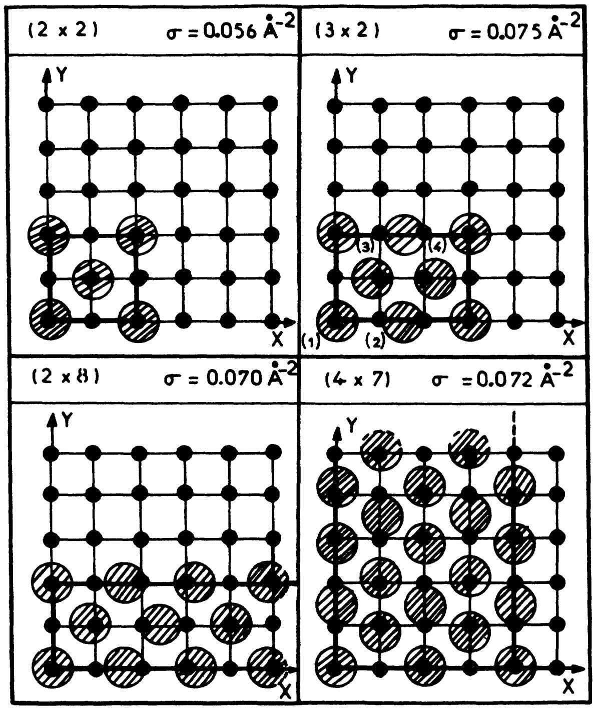

FIG. 2. Selected structures ($n_1 \times n_2$) of the Kr monolayer adsorbed on the MgO substrate. Same caption as for Fig. 1.

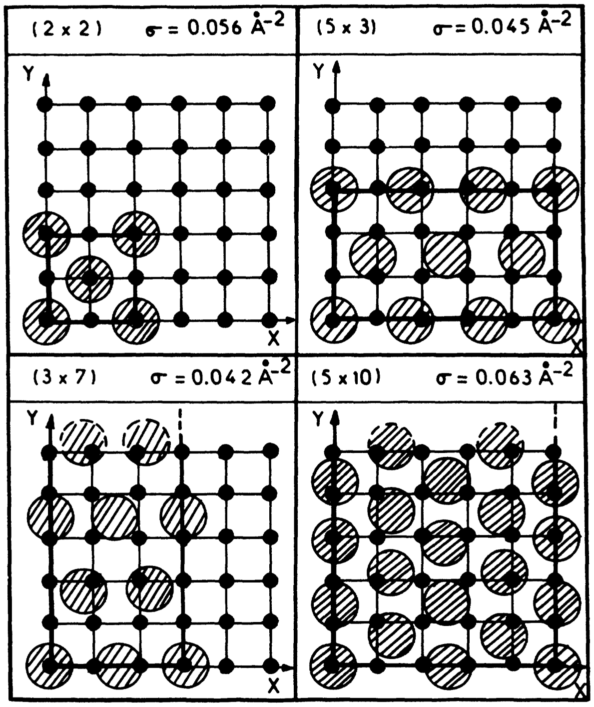

FIG. 3. Selected structures ($n_1 \times n_2$) of the Xe monolayer adsorbed on the MgO substrate. Same as for Fig. 1.

III. EXPERIMENTS

A. Measurements

1. Experimental setup and sample preparation

The experiments have been performed in an ultrahigh-vacuum (UHV) chamber (base pressure $<1\times10^{-10}$ torr) equipped with a four-grid LEED apparatus allowing the use of a 0.25-mm-diam low-intensity electron beam ($I \simeq 10^{-9}$ A). The diffracted beams are amplified with a channel-plane intensifier and observed on a flat fluorescent screen.[44,45] Gases are introduced in the UHV chamber through a leak valve and pressures are measured within the (10^{-10}–10^{-5})-torr range with an ionization gauge calibrated against a baratron.[45] The sample holder allows the MgO single crystal to be cooled to 20 K with a temperature regulation of 0.1 K or better. The temperature is measured with a platinum resistor (100 Ω at 273 K). The absolute-surface-temperature calibration has been done using the bulk-condensation vapor pressures of the different adsorbates studied in the present work.[13,46] Gases from Messer Griesheim, Düsseldorf, are 99.999%-pure grade for argon and 99.99% pure for krypton and xenon. A mass spectrometer allows us to monitor the concentration of background impurities before and after introducing the gas. All impurities have relative concentration lower than 10^{-3} at a total pressure of 10^{-8} torr and lower than 10^{-4} at 10^{-5} torr. They consist mostly of molecular hydrogen. In order to achieve that level of purity, we pump continuously on the chamber with a turbomolecular pump while introducing the gas, the pressure of which is maintained constant by adjusting the leak valve.

The MgO single crystals from Spicer (99.9% grade) are cleaved and mounted on the sample holder in a glove box under a dry nitrogen atmosphere after which they are transferred to the UHV chamber. During the transfer, helium gas is blown onto the crystal surface until it reaches the chamber, which is full of dry nitrogen. Then, the chamber is pumped out and baked to 200 °C for 24 h. During the baking procedure, the MgO is heated to 300 °C. When the UHV conditions have been obtained ($p<1\times10^{-10}$ torr), the MgO is heated to ~450–500 °C for 15 h. This crystal treatment allows us to get sharp LEED diffraction patterns at energies above 50 eV. If the crystal is cleaved in the air and transferred rapidly to the chamber, LEED patters are observable above 200 eV only, leaving an intense background below this energy. Furthermore, superstructure spots from an adsorbed monolayer can be observed only if the above-mentioned treatment has been done. On an air-cleaved sample, no overlayer pattern is observed. Increasing the adsorbate gas pressure in the chamber results in an increase of the background intensity until the MgO LEED pattern disappears due to bulk adsorbate condensation.

2. *Structure determination*

The overlayer structure determination and the lattice-parameter measurements are obtained from photographs taken with a Nikon 35-mm *f*/5.6 camera, using Ilford HP5 films (500 ASA). Exposure times are 5–10 s for the bare MgO surface and 30–60 s for the rare-gas overlayers. All our measurements are corrected for flat screen distortions. They are normalized to known reference distances of the MgO(100) surface plane. Measurements of angles between spot directions are straightforward and do not need any correction for an incoming beam perpendicular to the sample surface. The relative accuracy on the distance determinations is about 2%. The absolute accuracy on the angle measurements is about 1°.

3. *LEED adsorption isotherms and isobars*

Adsorption isotherms (isobars) giving the amount adsorbed versus gas pressure (temperature) at a given temperature (pressure) are obtained by measuring directly on the screen the decrease of the intensity of a MgO LEED diffraction spot using a linear photometer with a 6′ aperture angle. We assume that, within monolayer condensation, the decrease of the intensity of a substrate diffraction spot is proportional to the amount adsorbed.[6] This method is commonly used with physisorbed systems.[45,47,48] When 3D crystallites grow, the intensity decreases exponentially with time at supersaturation.

When stepwise isotherms (isobars) are observed, the amount adsorbed is normalized to the plateau of first-layer condensation, which is taken as coverage $\Theta = 1$ monolayer (ML).

B. Results

In the following subsections we will present the experimental results for argon, krypton, and xenon in the monolayer regime. The multilayer experiment will be reported elsewhere.[13,46]

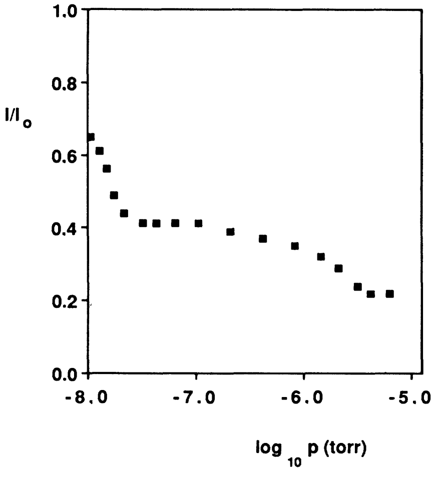

FIG. 4. LEED photometric isotherm of argon on MgO(100) at $T = 32.2$ K. Electron energy is 146 eV. I/I_0 represents the intensity I of the MgO 10 spot vs Ar pressure normalized to its value I_0 at zero coverage. The plateau features monolayer condensation. Bulk condensation pressure is $p_0 = 1 \times 10^{-5}$ torr.

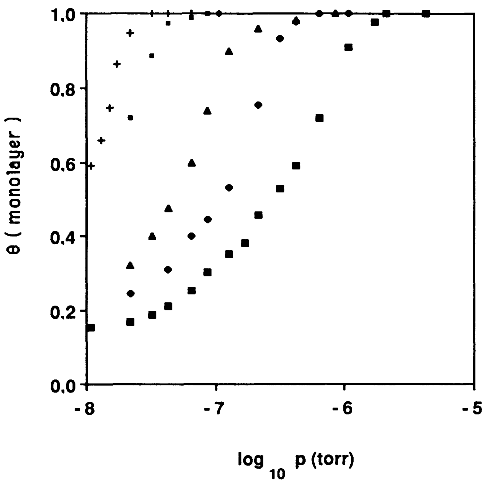

FIG. 5. Adsorption isotherms of Ar on MgO(100) in the monolayer range. +, 32.2 K; ■, 32.5 K; ▲, 33.7 K; ◆, 34.6 K; ■, 35.6 K. These experimental points are obtained from photometric isotherms such as Fig. 4, taking the coverage $\Theta = 1$ ML at the plateau.

1. *Argon*

We have studied the condensation of the argon monolayer in the pressure range 10^{-8}–10^{-5} torr and temperature range 25–36 K. Figure 4 shows a LEED photometric isotherm at $T = 32$ K. This isotherm features a sharp decrease of the MgO 10 spot corresponding to the condensation of the first argon monolayer. It is followed by a plateau along which the intensity is approximately constant within more than 1 order of magnitude in pressure. Hence, along the plateau, the argon coverage remains approximately constant. We take this coverage

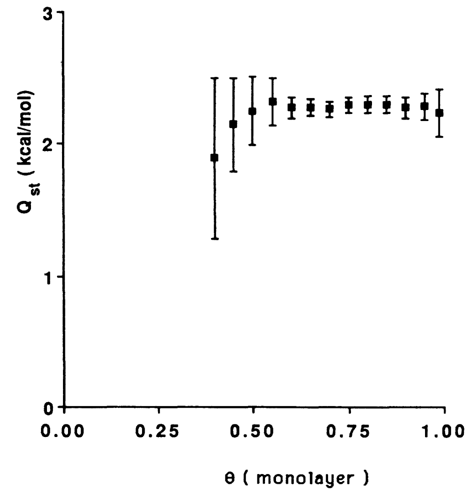

FIG. 6. Isosteric heat of condensation of Ar on MgO(100) for coverages ≤ 1 ML, $25 < T < 36$ K.

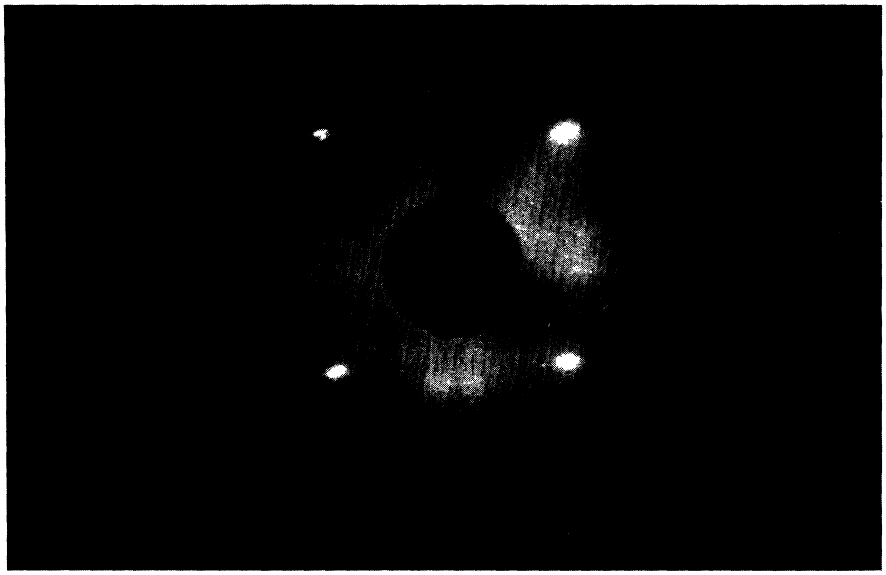

FIG. 7. LEED pattern of an Ar monolayer adsorbed on MgO(100) at $T=35$ K and $p\simeq 1.1\times 10^{-6}$ torr. Electron energy is 113.5 eV. The four main spots are from MgO. The doublets between MgO spots are from the Ar $2\times n$ $(n\simeq 3)$ overlayer. Multiple diffraction spots are clearly visible close to the center of the pattern.

Θ equal to 1 ML and normalize the amount adsorbed to its intensity value. This isotherm also shows second-layer condensation, which will be described in another paper.[46]

We show in Fig. 5 a set of normalized adsorption isotherms in the monolayer regime. They are reversible and reproducible. Six different adsorption isotherms and three isobars have been measured. They allow us to determine the isosteric heat of condensation q_{st} at different coverages Θ. We have

$$q_{\mathrm{st}}=-R\left[\frac{d\ln p}{d(1/T)}\right]_{\Theta}. \tag{16}$$

The variation of q_{st} versus coverage Θ is shown in Fig. 6. One can see that q_{st} is approximately constant and equal to 2.3 ± 0.3 kcal/mol for $0.50<\Theta<1$. This value is to be compared to that found by Madih[11] on MgO powders at higher temperature $(49<T<66$ K), that is, $q_{\mathrm{st}}=2.00\pm 0.03$ kcal/mol. In this high-temperature experiment, q_{st} is associated with a 3D gas$\rightarrow$2D liquid transition, whereas in our experiments the transition is 3D gas$\rightarrow$3D solid [the 2D triple point being estimated at $T_t(\mathrm{2D})\simeq 40$ K], which explains the higher value of q_{st}.

We observe the appearance of argon superstructure spots on the LEED pattern when coverage reaches $\Theta\simeq 0.75$. The most favorable electron energy is 115 eV. The pattern is also visible at 70–80 eV. A typical LEED pattern at $T=35$ K and $p=1.1\times 10^{-6}$ torr is shown in Fig. 7. It corresponds to $\Theta\simeq 1$ and features four main sets of doublets between MgO spots plus four other sets of doublets closer to the center of the pattern. These inner spots are interpreted as multiple-diffraction spots. They are much less intense than the outer spots. Up to second-layer condensation, the LEED patterns remain qualitatively identical. Only the positions of the spots change.

The overlayer structure compatible with these patterns is an uniaxially commensurate $2\times n$ solid phase, argon atoms being located in the troughs along the [110] rows of Mg ions. Two domains may exist on the MgO surface oriented 90° apart. They give the doublets in the LEED

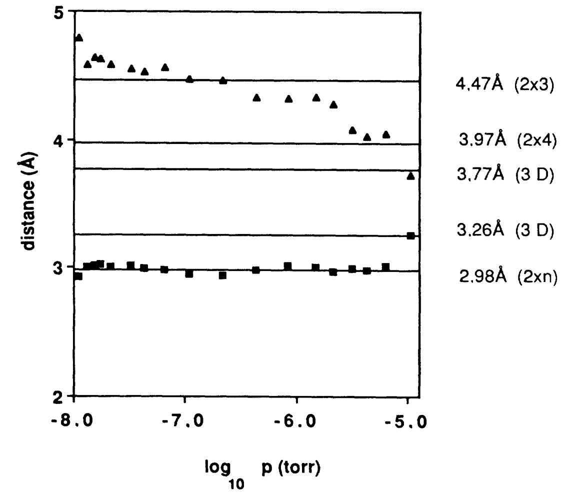

FIG. 8. The distance X (■) and Y (▲) in an Ar monolayer on MgO(100) vs the logarithm of the Ar pressure at $T=32.2$ K (see Fig. 9). The distance X remains constant up to second-layer condensation (see Fig. 4 for the corresponding isotherm), giving clear evidence that Ar atoms remain in the surface troughs. The variation of Y represents the uniaxial compression along the troughs.

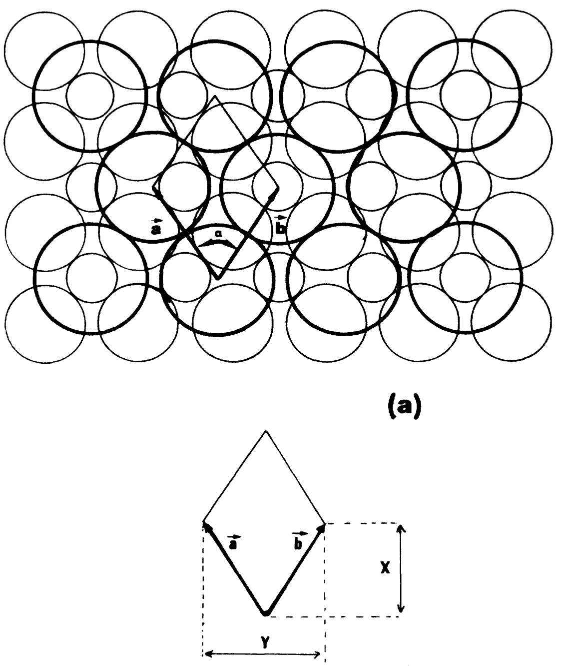

FIG. 9. (a) Schematic representation of the 2×4 Ar commensurate overlayer on MgO(100). The light circles stand for O (large) and Mg (small) atoms. The heavy large circles stand for Ar atoms. The unit cell of the Ar overlayer is shown by **a** and **b**. $\alpha=67.34°$ and $a=b=3.58$ Å. For the 2×3 structure $\alpha=73.74°$ and $a=b=3.72$ Å. (b) The X and Y distances.

pattern.[14] Figure 8 shows the variation of the distance X between argon rows parallel to the troughs and distance Y between atoms along the troughs versus the logarithm of the pressure at $T=32.2$ K. The particular values $X=2.98$ Å (distance between Mg channels), $Y=4.47$ Å (2×3 structure), and $Y=3.97$ Å (2×4 structure) are shown by dark horizontal lines. The corresponding adsorption isotherm is represented on Fig. 4.

From these observations we can conclude that the $2\times n$ commensurate solid overlayer is uniaxially compressed when the chemical potential increases from a structure close to the 2×3 at submonolayer coverage to a structure close to the 2×4 at second-layer condensation. These structures have already been shown in Fig. 1. Figure 9(a) shows the 2×4 commensurate structure together with the corresponding unit cells. X and Y are clearly indicated in Fig. 9(b). This behavior is qualitatively identical in the temperature and pressure range studied. A detailed analysis of the parameter versus chemical potentials will be given elsewhere.[13,46] The observation of the 2×3 commensurate structure at submonolayer coverage agrees with the neutron-diffraction results of Madih.[11] However, Madih reports the observation of a hexagonal packing before second-layer condensation, in disagreement with our results.

2. *Krypton*

The condensation of the krypton monolayer has been studied in the $(10^{-9}-10^{-6})$-torr pressure range and the temperature range $41<T<48$ K. Figure 10 shows an adsorption isotherm at 43.3 K up to second-layer formation. As for argon, we will focus our attention on the monolayer regime only. We observed again a sharp decrease of the MgO 10 spot intensity followed by a plateau. This behavior indicates that a krypton monolayer is condensed which is stable at almost 2 orders of magnitude in pressure. As before, we take this plateau intensity as that of the coverage one and normalize the intensities to it. Figure 11 represents a set of five adsorption isotherms in the monolayer regime. They are reversible and reproducible. We have determined the isosteric heat of condensation q_{st} at different coverages as shown in Fig. 12. As for argon, q_{st} remains approximately constant for coverages between 0.5 and 1 ML. Its value is

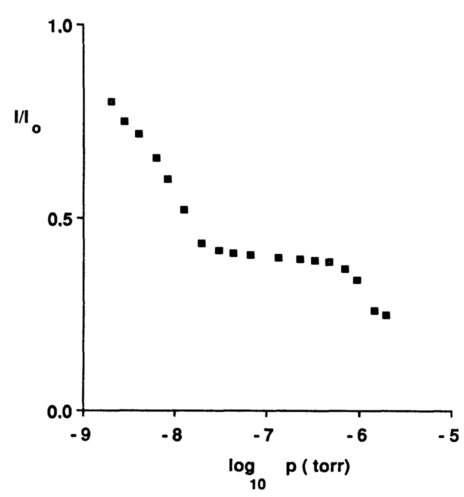

FIG. 10. LEED photometric isotherm of Kr on MgO(100) at $T=43.3$ K. Electron energy is 146 eV. $p_0=2.3\times10^{-6}$ torr. See Fig. 4 for explanations.

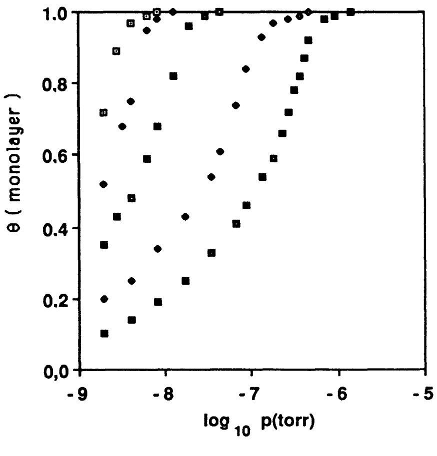

FIG. 11. Adsorption isotherms of Kr on MgO(100) in the monolayer range. □, 41 K; ♦, 41.8 K; ■, 43.3 K; ◇, 45.1 K; ■, 47.4 K. See Fig. 5 for comments.

$q_{st} = 3.1 \pm 0.2$ kcal/mol, in good agreement with the value obtained at higher temperature ($66.7 < T < 99$ K) by Coulomb *et al.*,[9] 2.8 ± 0.1 kcal/mol. As for argon, our experiments are performed below the 2D triple point [$T_t(2D) \simeq 66.6$ K], which explains our higher value of q_{st}.

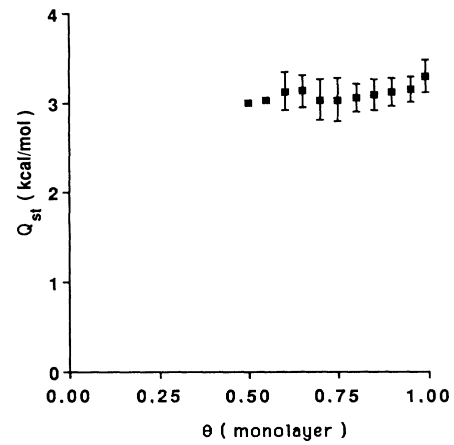

FIG. 12. Isosteric heat of condensation of Kr on MgO(100) for coverages ≤ 1 ML and $41 < T < 48$ K.

The first LEED superstructure spots appear for $\Theta \simeq 0.75$. The most favorable electron energies are 65, 85, and 115 eV. Figure 13 shows a LEED pattern at $T = 41.8$ K and $p = 1.2 \times 10^{-8}$ torr, that is, $\Theta \simeq 1$. It features a weak ring on which four sets of doublets are superimposed. The intensity of the ring, as well as that of the doublets, increases further with increasing pressure along the plateau of the isotherm. We interpret these observations as evidence of a hexagonal solid monolayer with orientational disorder (ring) coexisting with a commensurate $2 \times n$ solid phase analogous to that of argon. We find that the positions of the doublets are in reasonable agreement with a 2×8 structure. However, the $2 \times n$ structure presents a continuous variation of the distance along the Mg channels with increasing pressure along the plateau of the isotherm.[13,46] The d spacing versus pressure, deduced from the diameter of the ring or the position of the doublets at $T = 41.8$ K, is represented in Fig. 14(a), as well as the corresponding adsorption isotherm, Fig. 14(b). If we assume, as said above, a hexagonal packing of the krypton atoms, it corresponds to the distance d_{10}. Hence the distance between atoms varies from 4.27 to 4.19 Å with increasing pressure along the plateau of the isotherm. Such distances are 4–6 % larger than those between atoms in a (111) plane of bulk krypton. It is likely, then, that either the surface corrugation or heterogeneities are responsible for this monolayer expansion. Although the purpose of this paper is the study of monolayer behavior, it is worth noticing that the d spacing at second-layer condensation corresponds well to that of a (111) plane of bulk krypton.[13,46] Our results are somewhat different from those reported by Jordan *et al.*[12] on MgO powders using x-ray diffraction as a probe. For coverage 1.1, these authors find a hexagonal packing only with a d spacing very close to that of bulk (111) planes. However, their experiments show very poor MgO surface quality, as indicated by the very low coherence length of their krypton overlayer (<20 Å). Furthermore, they cannot distinguish between the hexagonal and $2 \times n$ structures within the scattering-wave-

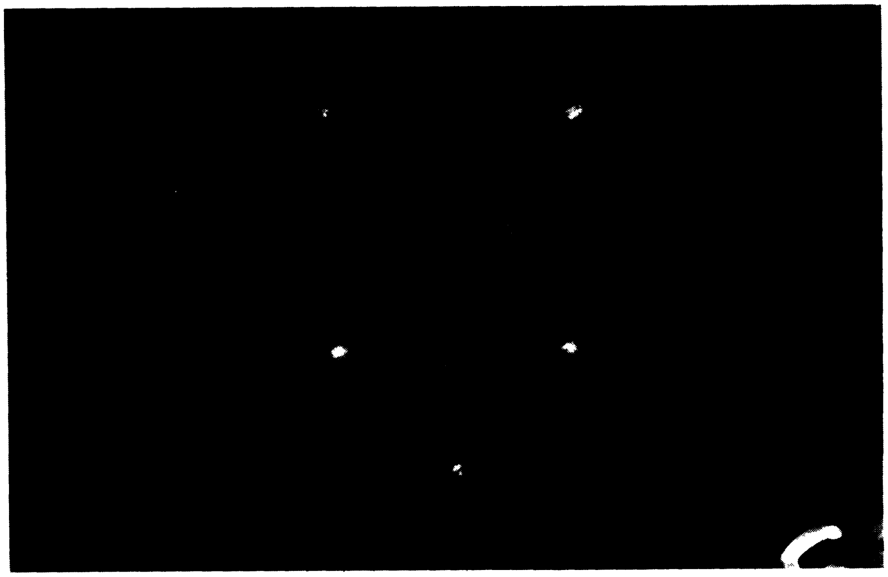

FIG. 13. LEED pattern of a krypton monolayer adsorbed on MgO(100) at $T = 41.8$ K and $P = 1.2 \times 10^{-8}$ torr. Electron energy is 115.7 eV. As for Fig. 7, the most intense spots are from MgO. The Kr overlayer gives a weak ring, on which are superimposed four sets of doublets. The ring is probably due to a hexagonal packing of Kr atoms with crystallites orientationally disordered coexisting with a $2 \times n$ ($n \simeq 8$) structure (doublets).

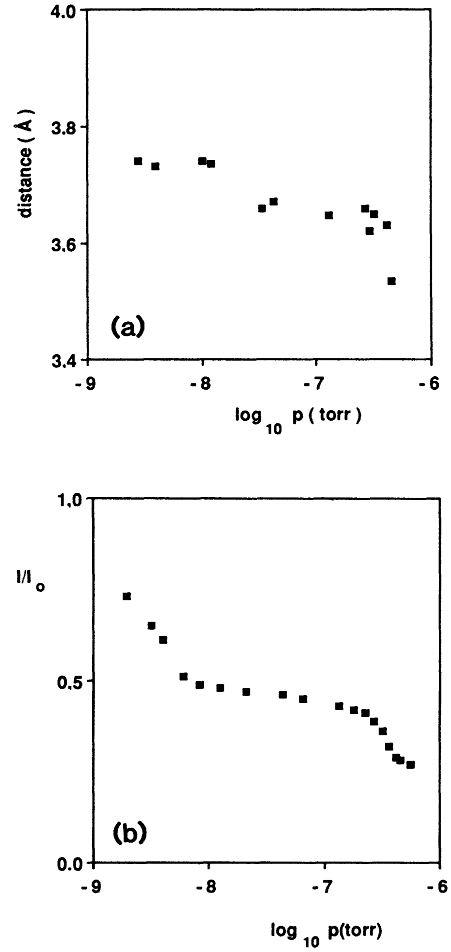

FIG. 14. (a) d spacing vs pressure as deduced from the diameter of the ring observed in the LEED pattern (on Fig. 13) for a Kr monolayer at $T=41.8$ K. (b) LEED photometric isotherm under the same conditions as in (a).

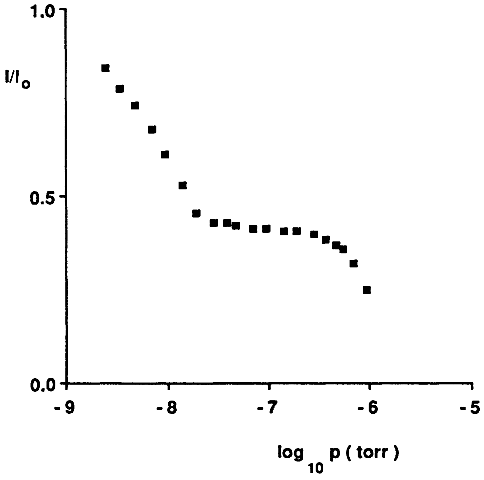

FIG. 15. LEED photometric isotherm of Xe on MgO(100) at $T=58.3$ K. Electron energy is 146 eV. $p_0=1\times10^{-6}$ torr. See Fig. 4 for explanations.

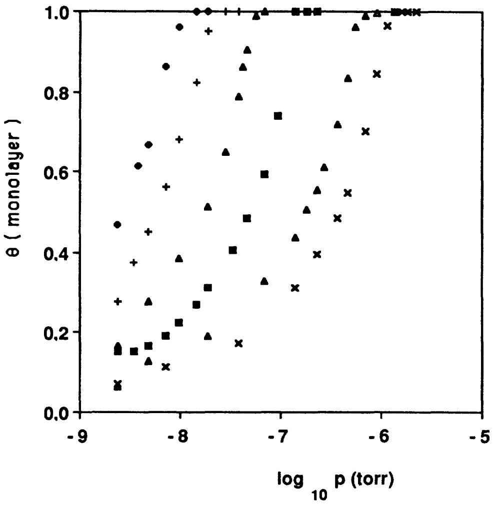

FIG. 16. Adsorption isotherms of Xe and MgO(100) in the monolayer range. ♦, 57.2 K; +, 58.3 K; ▲, 59.6 K; ■, 62.1 K; △, 65 K; ×, 66.3 K. See Fig. 5 for comments.

vector range investigated as long as the two d spacings, that of the ring and that of the doublets, are close enough.

3. *Xenon*

We have investigated xenon monolayer condensation in the temperature and pressure ranges $56<T<67$ K and $10^{-9}<p<5\times10^{-6}$ torr. Figure 15 shows an adsorption isotherm at $T=58.3$ K up to second-layer condensation. The general behavior is similar to that of argon and krypton. The sharp drop of the 10 MgO spot intensity features monolayer adsorption. It is followed by a plateau that we take as coverage one. The measurements are reversible and reproducible. Figure 16 represents a set of six adsorption isotherms. The isosteric heat of con-

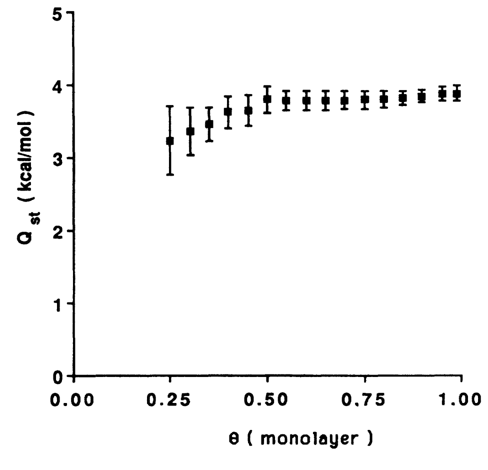

FIG. 17. Isosteric heat of condensation of Xe on MgO(100) for coverages ≤ 1 ML and $56<T<67$ K.

densation q_{st} has been determined versus coverage. Its variation is shown in Fig. 17. The value of q_{st} remains approximately constant for $0.5 < \Theta < 1$ and equal to $q_{\mathrm{st}} = 3.85 \pm 0.15$ kcal/mol, in good agreement with that measured by Coulomb *et al.*[9] on MgO powders at higher temperature ($96 < T < 132$ K), that is, 3.7 ± 0.15 kcal/mol. As for the other two gases, our experiments are performed below the 2D triple-point temperature of 100.8 K.

The overlayer LEED pattern appears when $\Theta \simeq 0.8$. Figure 18 shows a LEED pattern at $T = 62.1$ K and $p_{\mathrm{Xe}} = 2.6 \times 10^{-7}$ torr at two different electron energies, 89.3 and 118.9 eV, and a coverage of 1 ML (beginning of the plateau of the isotherm, see Fig. 16). At low energies ($\simeq 90$ eV), the LEED pattern features are streaks in the [11] and [$\bar{1}$1] MgO surface directions, intersecting at the 00 spot. These streaks present an enhanced intensity at approximately half the distance between MgO spots, that is, around the position of the doublets observed with krypton or argon. At higher energy (115–120 eV) the streaks are barely visible, but a ring can be observed with a higher intensity in the [11] and [$\bar{1}$1] directions. The presence of streaks can be interpreted as evidence of an important loss of order in the [11] surface direction of MgO (or the [100] bulk direction). We think that the ring, as for krypton, indicates a hexagonal packing of xenon atoms with orientational disorder of the 2D xenon crystallites. With this hypothesis, the diameter of the

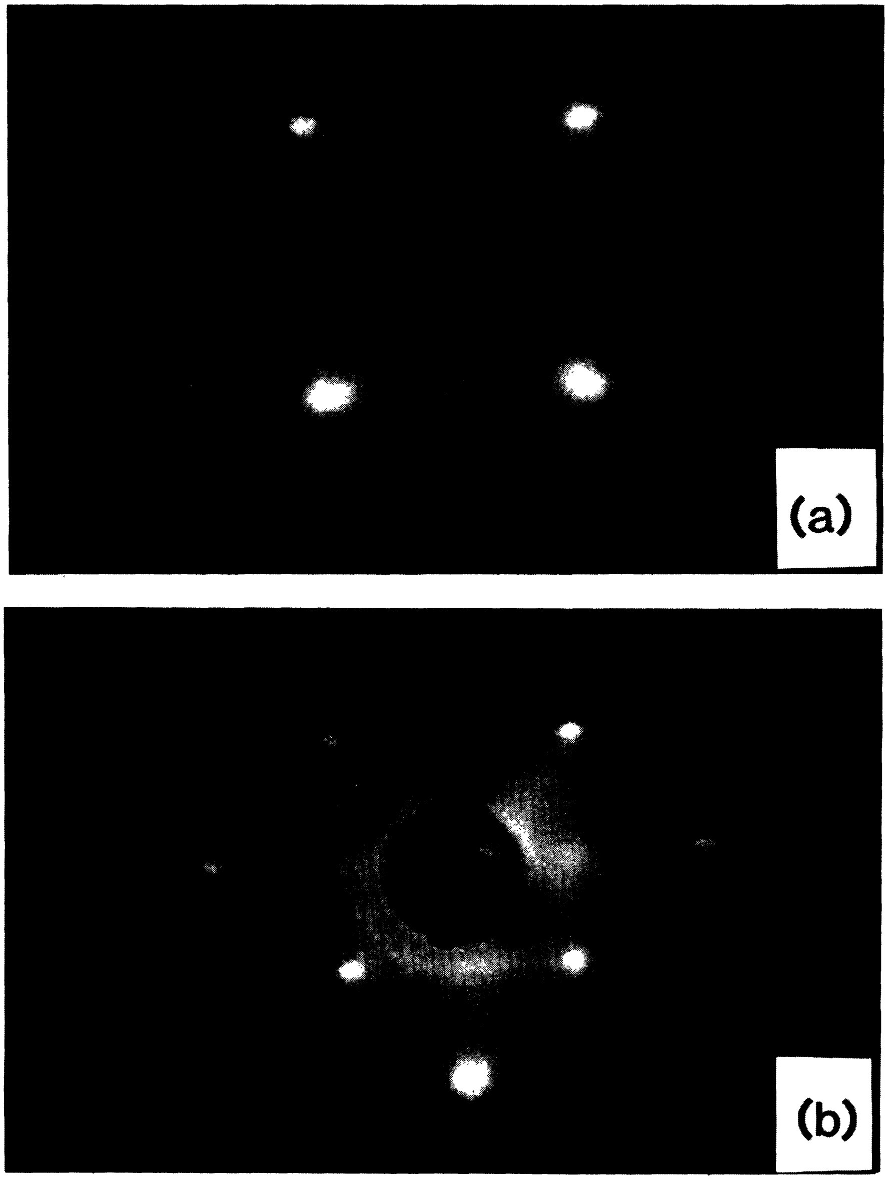

FIG. 18. LEED patterns of a Xe monolayer adsorbed on MgO(100) at $T = 62.1$ K and $p = 2.6 \times 10^{-7}$ torr. Electrons energies are (a) 89.3 eV and (b) 118.9 eV. The streaks, (a), in the $\bar{1}1$ and $\bar{1}1$ surface directions indicate an important loss of order in those directions. The ring observed at higher energy, (b), is probably due to a hexagonal packing of Xe atoms.

ring corresponds to the distance d_{10}. It is equal to an average value of 3.99±0.1 Å and remains approximately constant within our experimental accuracy along the plateau of the isotherm. The distance between nearest neighbors is about 4.6±0.15 Å. This value is to be compared to that of the (111) plane of bulk Xe, which is equal[49] to 4.37 Å at 60 K. It is worthwhile mentioning that a thick film of xenon on MgO gives a modulated ring from which we determine a d_{10} spacing of 3.8±0.17 Å, that is, a nearest-neighbor distance of 4.4±0.1 Å, in close agreement with that of bulk xenon.

As a summary for the xenon experiments, the xenon overlayer is incommensurate with the MgO surface. There is strong evidence that the packing is hexagonal with a lower density than in the (111) plane of the bulk and with an important disorder in the [11] surface direction. It is interesting to note that it is along that direction that MgO surface steps align.[50] This could be a reason for the disorder. Another more interesting reason could be the frustration phenomenon itself between the square symmetry of the (100) MgO surface and the hexagonal symmetry that the adsorbate prefers to adopt.

IV. COMPARISON BETWEEN CALCULATIONS AND EXPERIMENTS

A. Argon monolayer

At a coverage ratio close to 1, the experimentally observed structure of argon adsorbed on the MgO substrate is clearly interpreted by the calculations. When pressure rises, this 2×3 structure evolves up to the 2×4 structure with intermediate structures of the type $2\times n_2$ $(n_2>4)$. This result is in good agreement with the calculated trends. Indeed, it is shown that the 2×4 structure corresponds to a slightly compressed one with respect to the hexagonal structure. Such a geometry cannot be stable unless if it gains energy by compression, as observed. The intermediate structures $2\times n_2$ have been investigated in our calculations (Table VIII). They correspond to structures with a number density closer and closer to the hexagonal one. They are slightly less stable than the 2×3 one under normal pressure conditions, but they could reach a greater stability under compression. Note also that when the 2×4 structure occurs, the bilayer tends to be formed, which can be responsible for increasing stability of the 2×4 compressed structure. Our calculations cannot take into account the influence of the second layer on the monolayer stability.

TABLE VIII. Structures $(2\times n_2)$ for the Ar monolayer adsorbed on MgO.

Structure $(n_1\times n_2)$	Density σ (Å^{-2})	Static energy (meV)	q (kcal mol^{-1}) ($T=30$ K)
(2×3)	0.075	−124.75	2.324
(2×10)	0.078	−124.53	2.319
(2×7)	0.0804	−124.18	2.311
(2×11)	0.082	−123.71	2.30
(2×4)	0.084	−122.43	2.27

Moreover, the calculated and experimental heats of adsorption for the Ar monolayer are compared in Table VII. The calculation corresponds to the more stable 2×3 structure, at $T=30$ K. The calculated value satisfactorily agrees with the measured one, in spite of the uncertainties provided by the use of an harmonic model for the monolayer dynamics. It is also probable that the value of the Grüneisen constant underestimates the adsorption energy.

B. Krypton monolayer

Because of less clear LEED information, the interpretation is slightly more ambiguous in the krypton case. The observed ring and doublets could be a superimposition of the signals due to the hexagonal and 2×8 structures. These structures have parameters and angles close to the observed one. The calculations can interpret the presence of the 2×2 and 2×8 structures, but not the occurrence of the hexagonal one. Such a discrepancy requires involvement of another cause of stabilization, such as surface defects. It could also be due to inaccuracies in the chosen atom-substrate potential, which would induce an overestimate of the energy corrugation. The isosteric heat q_{st} has been calculated for the 2×8 structure and yields a value close to the measured one. Dynamical corrections of the static energy show that the hexagonal structure can gain several meV of energy with respect to the 2×8 structure, but it still cannot compete with the 2×2 and 2×8 structures, except for the above-mentioned additional effects.

C. Xenon monolayer

From the LEED pattern, we deduce a uniaxial disordered hexagonal structure. The disorder is evidenced by the observed streaks along the [100] direction. The calculation shows a small energy difference (∼10 meV) between the square 2×2 and nearly hexagonal 5×10 structures in favor of the 2×2 one. Here, again, as for Kr, the stabilization of the hexagonal phase can be due to the already-mentioned causes (defects and potential inaccuracy). The calculated isosteric heat q_{st} (cf. Table VII) agrees well with the experimental result.

V. CONCLUSIONS

The LEED measurements of the structure and adsorption energy of rare-gas monolayers adsorbed on a square MgO(100) substrate exhibit typical frustration phenomena. The frustration is clearly evidenced for the Ar monolayer, where the surface troughs along the [110] directions impose a commensurate $2\times n$ structure of the overlayer. For the other rare-gas monolayers the main point is the appearance of the hexagonal structure, showing a lesser influence of the substrate corrugation.

The calculations of the more stable monolayer structures are able to interpret the main aspects of the experimental results, and the estimated isosteric adsorption heats are close to the measured values. In particular, they show a small energy difference between the commensurate and incommensurate phases for the heavier rare gases. Several experimental problems nevertheless remain; they are connected to the presence of mechanical (steps) or chemical (H_2O contamination) defects at the substrate surface. These undesirable effects could be eliminated by vacuum cleavage of the MgO crystal and more higher-temperature annealing of the substrate surface.

Regarding the calculations, several drawbacks connected to the approximate formulation of the monolayer dynamics could be eliminated. Indeed, the harmonic or quasiharmonic approximation is far from accurate at temperatures higher than 40–50 K. Though the temperature effect provides a small correction of the static one for strongly corrugated crystals, errors of several meV can be expected within the framework of the harmonic Debye model. Moreover, the coupled dynamics of the monolayer (coupling of the perpendicular and in-plane motions) and of the substrate can also yield additional contributions to the adsorption heat. Another point of special emphasis is connected to the influence of the bilayer formation on the monolayer stability. Keeping in mind that crucial problems such as the accuracy of the potential parameters and the presence of surface defects are far from solved, it is nevertheless interesting, from a conceptual point of view, to improve the dynamical treatment and to include the influence of the bilayer. This is deferred to a subsequent paper.

ACKNOWLEDGMENTS

The Laboratoires de Physique Moléculaire de l'Université de Besançon and des Surfaces-Interfaces de l'Université d'Aix-Marseille II are associated with the Centre National de la Recherche Scientifique, unités associées Nrs. 772 and 794, respectively.

APPENDIX: POTENTIAL EXPANSION FOR THE STATICS

The interaction potential energy of the monolayer is written as

$$V_M = N \sum_{l,s,s'} \sum_{m} \frac{C^m}{[\mathbf{R}(l)+\tau(s')-\tau(s)]^m} \left[1 + \frac{m}{4} \frac{[z(s')-z(s)]^2}{[\mathbf{R}(l)+\tau(s')-\tau(s)]^2} + \cdots \right] , \tag{A1}$$

where $m = 6, 8, \ldots$ for the binary dispersion contribution and $m = 12, 14, \ldots$ for the binary repulsion term. The many-body interaction can be taken into account by an effective potential with $m = 9$. N defines the number of primitive supercells of the monolayer.

The monolayer substrate potential is separated into four contributions:

$$V_{MS} = \bar{v}_b + \tilde{v}_b + V_m + v_i \ . \tag{A2}$$

$\bar{v}_b$ defines the continuum contribution of the pairwise adsorbate-substrate potential expanded as

$$\bar{v}_b = \frac{2\pi}{S} N \sum_{p,r} \sum_{s} \sum_{m'} \frac{C^{m'}(r)}{(m'-2)(d^*+pL)^{m'-2}} \left[1 - \frac{m'-2}{d^*+pL} z(s) + \frac{(m'-1)(m'-2)}{2(d^*+pL)^2} z^2(s) + \cdots \right] . \tag{A3}$$

N/S characterizes the number of primitive supercells per surface unit, $m' = 4, 6, \ldots$ for the adsorbate-substrate dispersion term and $m' = 10, 12, \ldots$ for the repulsion one. p labels an additional index connected to the sum over the substrate planes parallel to the surface (the surface plane is defined as $p = 0$) and L is the distance between two consecutive planes p and $p+1$. The pairwise adsorbate-substrate potential $\tilde{v}_b$, which accounts for the discrete nature of the substrate, is expanded in a similar way:

$$\begin{aligned} \tilde{v}_b = \frac{4\pi N}{S} \sum_{p,r} \sum_{s} \sum_{\mathbf{g}} \sum_{m'} & \frac{C^{m'}(r)(g/2)^{m'/2-1}}{(m'/2-1)!(d^*+pL)^{m'/2-1}} \\ & \times \cos(\mathbf{g}\cdot\tau_l - \mathbf{g}\cdot\tau_{r,p}) \left[K_{m'/2-1}(g(d^*+pL)) - g k_{m'/2}(g(d^*+pL)) z(s) \right. \\ & \left. \qquad - \frac{g}{2} \left[-\frac{1}{d^*+pL} K_{m'/2}(g(d^*+pL)) - g K_{m'/2+1}(g(d^*+pL)) \right] z^2(s) + \cdots \right] . \end{aligned} \tag{A4}$$

K is the modified Bessel function of integer number and g characterizes the 2D reciprocal-lattice vector of the isolated substrate described by successive atomic planes:

$$\mathbf{g} = (2\pi/a)(g_1, g_2) , \tag{A5}$$

where g_1 and g_2 are integer numbers. Note that the cosine term in Eq. (A4) depends on the relative location of a given atom r in a plane p with respect to the same atom in the surface plane.

The remaining contributions V_m and v_i in Eq. (A2) characterize the continuum part of the substrate-mediated energy and the induction contribution, respectively. This second contribution is totally discrete since it characterizes the electric field created by the substrate ions and experienced by the monolayer. In contrast, the substrate-mediated energy contains continuum and discrete terms and only the continuum terms described by V_m will be considered here. V_m and v_i are, in fact, small additional contributions to V_{MS} and their dynamical influence is disregarded. Therefore V_m is written as

$$V_m = \frac{N}{2} \sum_{l} \sum_{s,s'} \tfrac{4}{3} C_{s_1} \eta_1(d^*) \frac{d^{*2} + |\mathbf{R}(l)+\tau(s')-\tau(s)|^2}{[4d^{*2} + |\mathbf{R}(l)+\tau(s')-\tau(s)|^2]^{3/2}[\mathbf{R}(l)+\tau(s')-\tau(s)]^3} - \frac{C_{s_2}\eta_2(d^*)}{[4d^{*2} + |\mathbf{R}(l)+\tau(s')-\tau(s)|^2]^3} . \tag{A6}$$

The parameters $C_{s_{1,2}}$ and $\eta_{1,2}(d^*)$ are defined in Table I. Note that, strictly speaking, $\eta_{1,2}$ depends on $D(s)$, but we will neglect this dependence for an estimate of V_m. At last, the induction potential is expressed as

$$v_i = -\frac{N}{2} \sum_{s} \alpha_M E^2(s) \tag{A7}$$

where the ionic field experienced by the sth rare-gas atom of the lth cell (polarizability α_M) is defined by its components:

$$\begin{aligned} E_x(s) &= -\frac{4\pi}{S} \sum_{p,r} \sum_{\mathbf{g}} \frac{L_p}{g} q_S(r) g_x e^{-g(d^*+pL)} \sin[\mathbf{g}\cdot(\tau_{(s)}-\tau_{rp})] , \\ E_y(s) &\equiv E_x(s) \text{ by replacing } g_x \text{ by } g_y , \\ E_z(s) &= -\frac{4\pi}{S} \sum_{p,r} \sum_{\mathbf{g}} \frac{L_p q_S(r)}{g} g e^{-g(d^*+pL)} \cos\{\mathbf{g}\cdot[\tau(s)-\tau_{rp}]\} . \end{aligned} \tag{A8}$$

The quantity L_p connected to a screening effect of the ionic charges $q_s(r)$ of the rth substrate atom has been defined in a previous paper. Equations (A1), (A3), (A4), (A6), and (A7) are then used to determine the literal expressions of the force F_T and the force constant ϕ_T in Eq. (5).

---

[1] A. Thomy and X. Duval, J. Chim. Phys. **66**, 1966 (1969); **67**, 286 (1970); **67**, 1101 (1970).

[2] M. Bienfait, Surf. Sci. **89**, 13 (1979), and references cited therein.

[3] G. L. Price and J. A. Venables, Surf. Sci. **49**, 264 (1975); H. M. Kramer, J. Cryst. Growth **33**, 65 (1976); A. Q. D. Faisal, M. Hamichi, G. Raynerd, and J. A. Venables, Phys. Rev. B **34**, 7740 (1986).

[4] J. L. Sequin, J. Suzanne, M. Bienfait, J. G. Dash, and J. A. Venables, Phys. Rev. Lett. **51**, 122 (1983); M. Bienfait, J. L. Seguin, J. Suzanne, E. Lerner, J. Krim, and J. G. Dash, Phys. Rev. B **29**, 983 (1984); J. A. Venables, J. L. Sequin, J. Suzanne, and M. Bienfait, Surf. Sci. **145**, 345 (1984).

[5] H. Hong and R. J. Birgeneau, Phys. Rev. B **33**, 3344 (1986); S. E. Nagler, P. M. Horn, T. F. Rosenbaum, R. J. Birgeneau, M. Sutton, S. G. J. Mochrie, D. E. Moncton, and R. Clarke, *ibid.* **32**, 7373 (1985), and references therein.

[6] J. Unguris, L. W. Bruch, E. R. Moog, and M. B. Webbs, Surf. Sci. **87**, 415 (1979); **109**, 522 (1981).

[7] J. Krim, J. G. Dash, and J. Suzanne, Phys. Rev. Lett. **52**, 640 (1984).

[8] A. Glachant, M. Jaubert, M. Bienfait, and G. Boato, Surf. Sci. **115**, 219 (1981).

[9] J. P. Coulomb, T. S. Sullivan, and O. E. Vilches, Phys. Rev. B **30**, 4753 (1984); J. P. Coulomb and O. E. Vilches, J. Phys. (Paris) **45**, 1381 (1984).

[10] J. P. Coulomb, K. Madih, and B. Croset, Phys. Rev. Lett. **54**, 1536 (1985).

[11] K. Madih, Ph.D. thesis, Université d'Aix-Marseille II, 1986.

[12] J. L. Jordan, J. P. McTague, J. B. Hastings, and L. Passell, Surf. Sci. **150**, L82 (1985).

[13] T. Meichel, Ph.D. thesis, Université d'Aix-Marseille II, 1987; T. Meichel and J. Suzanne (unpublished).

[14] T. Meichel, J. Suzanne, and J. M. Gay, C. R. Acad. Sci. Paris **303**, 69 (1986).

[15] J. M. Phillips and L. W. Bruch, Surf. Sci. **81**, 109 (1979).

[16] L. K. Moleko, B. Joos, T. M. Hakim, H. R. Glyde, and S. T. Chui, Phys. Rev. B **34**, 2815 (1986).

[17] G. L. Price and J. A. Venables, Surf. Sci. **59**, 509 (1976).

[18] B. Hall, D. L. Mills, and J. E. Black, Phys. Rev. B **32**, 4932 (1985).

[19] L. W. Bruch and J. A. Venables, Surf. Sci. **148**, 167 (1984).

[20] A. D. Novaco and J. P. McTague, Phys. Rev. Lett. **38**, 1286 (1977).

[21] J. Villain, Phys. Rev. Lett. **41**, 36 (1978).

[22] N. D. Shrimpton, B. Bergersen, and B. Joos, Phys. Rev. B **34**, 7334 (1986).

[23] B. Joos, B. Bergersen, and M. L. Klein, Phys. Rev. B **28**, 7219 (1983), and references therein.

[24] C. Girard and C. Girardet, Chem. Phys. Lett. **138**, 83 (1987).

[25] J. A. Barker, in *Rare Gas Solids I*, edited by M. L. Klein and J. A. Venables (Academic, New York, 1976), p. 212.

[26] R. J. Bell and I. J. Zucker, in *Rare Gas Solids I*, Ref. 25, p. 122.

[27] H. Y. Kim and M. W. Cole, Phys. Rev. B **35**, 3990 (1987).

[28] K. N. Jog, R. K. Singh, and S. P. Sanyal, Phys. Rev. B **31**, 6047 (1985).

[29] P. W. Fowler and J. M. Hutson, Surf. Sci. **165**, 289 (1986).

[30] S. C. Parker, Ph.D. thesis, University College, London, 1983.

[31] W. A. Steele, in *The Interaction of Gas with Solid Surfaces* (Pergamon, Oxford, 1974).

[32] L. W. Bruch and H. Watanabe, Surf. Sci. **65**, 619 (1977); L. W. Bruch, *ibid.* **125**, 194 (1983).

[33] G. Vidali and M. W. Cole, Surf. Sci. **110**, 10 (1981); M. W. Cole and J. R. Klein, *ibid.* **124**, 547 (1983).

[34] C. Girardet and C. Girard, Chem. Phys. Lett. **137**, 149 (1987).

[35] S. Rauber, J. R. Klein, M. W. Cole, and L. W. Bruch, Surf. Sci. **123**, 173 (1982).

[36] C. Girard and C. Girardet, Surf. Sci. **195**, 173 (1988), and references therein.

[37] M. R. Welton-Cook and M. Prutton, Surf. Sci. **64**, 633 (1977); **74**, 276 (1978).

[38] A. J. Martin and H. Bilz, Phys. Rev. B **19**, 6593 (1979); F. W. de Wette, W. Kress, and U. Schröder, *ibid.* **32**, 4143 (1985).

[39] F. W. de Wette, B. Firey, E. de Rouffignac, and G. P. Allredge, Phys. Rev. B **28**, 4744 (1983).

[40] C. Girardet and C. Girard, Phys. Rev. B (to be published).

[41] A. A. Maradudin, Rep. Prog. Phys. **28**, 331 (1965); R. J. Elliott, in *Lattice Dynamics and Intermolecular Forces,* edited by S. Califano (Academic, New York, 1975), p. 342.

[42] R. E. Cohen, L. L. Boyer, and M. J. Mehl, Phys. Rev. B **35**, 5749 (1987); W. Kress, F. W. de Wette, A. D. Kulkani, and U. Schröder, *ibid.* **35**, 5783 (1987).

[43] L. W. Bruch and M. S. Wei, Surf. Sci. **100**, 481 (1980); M. S. Wei and L. W. Bruch, J. Chem. Phys. **75**, 4130 (1981).

[44] S. Calisti, J. Suzanne, and J. A. Venables, Surf. Sci. **116**, 455 (1982).

[45] J. M. Gay, J. Suzanne, and R. Wang, J. Chem. Soc. Faraday Trans. 2 **82**, 1669 (1986).

[46] T. Meichel and J. Suzanne (unpublished).

[47] J. M. Gay, M. Bienfait, and J. Suzanne, J. Phys. (Paris) **45**, 1497 (1984).

[48] R. D. Diehl and S. C. Fain, J. Chem. Phys. **77**, 5065 (1982).

[49] G. L. Pollack, Rev. Mod. Phys. **36**, 748 (1964).

[50] J. M. Cowley and K. D. Neumann, Surf. Sci. **145**, 301 (1984).

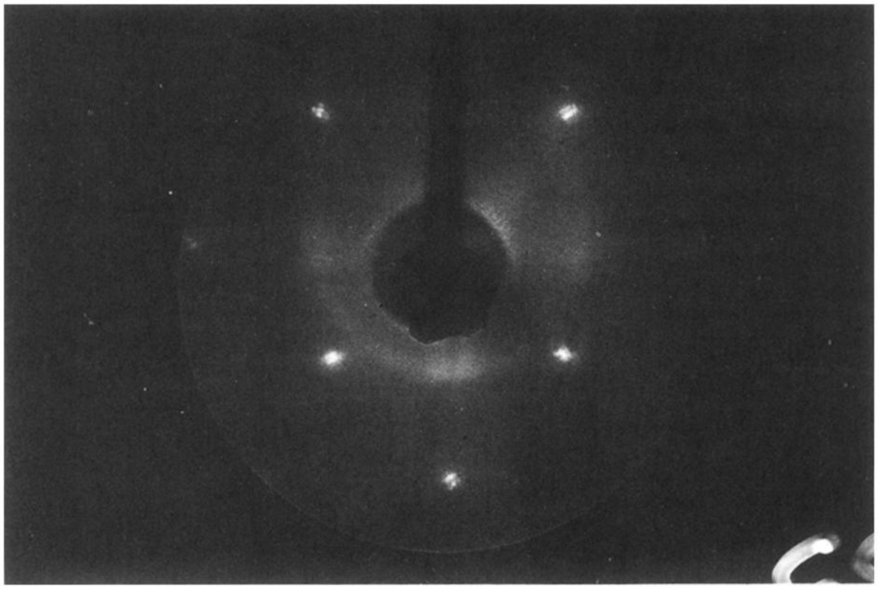

FIG. 13. LEED pattern of a krypton monolayer adsorbed on MgO(100) at $T = 41.8$ K and $P = 1.2\times10^{-8}$ torr. Electron energy is 115.7 eV. As for Fig. 7, the most intense spots are from MgO. The Kr overlayer gives a weak ring, on which are superimposed four sets of doublets. The ring is probably due to a hexagonal packing of Kr atoms with crystallites orientationally disordered coexisting with a $2\times n$ ($n \simeq 8$) structure (doublets).

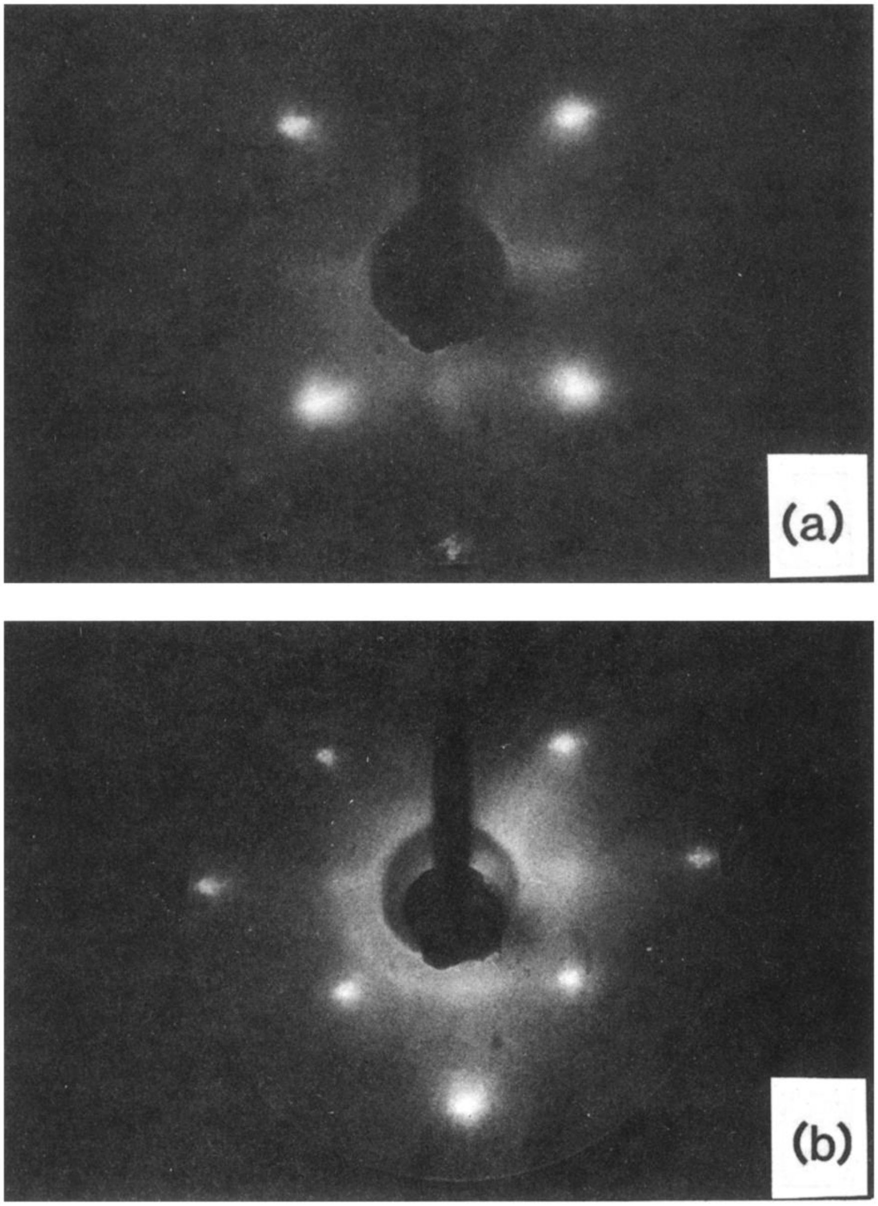

FIG. 18. LEED patterns of a Xe monolayer adsorbed on MgO(100) at $T=62.1$ K and $p=2.6\times10^{-7}$ torr. Electrons energies are (a) 89.3 eV and (b) 118.9 eV. The streaks, (a), in the $\bar{1}1$ and $\bar{1}1$ surface directions indicate an important loss of order in those directions. The ring observed at higher energy, (b), is probably due to a hexagonal packing of Xe atoms.

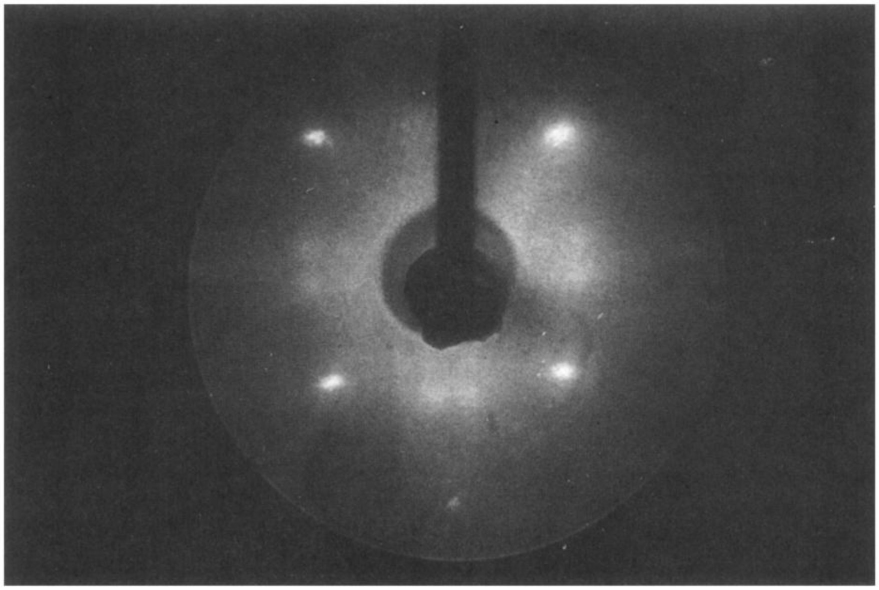

FIG. 7. LEED pattern of an Ar monolayer adsorbed on MgO(100) at $T = 35$ K and $p \simeq 1.1\times 10^{-6}$ torr. Electron energy is 113.5 eV. The four main spots are from MgO. The doublets between MgO spots are from the Ar $2\times n$ ($n \simeq 3$) overlayer. Multiple diffraction spots are clearly visible close to the center of the pattern.